Sizing Sub-Wavelength Defects with Ultrasonic Imagery: An Assessment of Super Resolution Imaging on Simulated Rough Defects

Joshua B. Elliott, Michael J. S. Lowe, Peter Huthwaite, Richard Phillips, and David J. Duxbury

***Abstract*—There is a constant drive within the nuclear power industry to improve upon the characterisation capabilities of current ultrasonic inspection techniques in order to improve safety and reduce costs. Particular emphasis has been placed on the ability to characterise very small defects which could result in extended component lifespan and help to reduce the frequency of in-service inspections. Super Resolution algorithms, also known as sampling methods, have been shown to demonstrate the capability to resolve scatterers separated by less than the diffraction limit when deployed in representative inspections and therefore could be used to tackle this issue. In this paper, the Factorization Method (FM) and the Time Reversal Multiple-Signal-Classification (TR-MUSIC) algorithms are applied to the simulated ultrasonic array inspection of small rough embedded planar defects to establish their characterisation capabilities. Their performance was compared to the conventional Total Focussing Method (TFM). A full 2D finite element Monte Carlo modelling study was conducted for defects with a range of sizes, orientations and magnitude of surface roughness. The results presented show that for sub-wavelength defects, both the FM and TR-MUSIC algorithms were able to size and estimate defect orientation accurately for smooth cases and for rough defects up to a roughness of 100 microns. This level of roughness is representative of thermal fatigue defects encountered in the nuclear power sector. This contrasted with the relatively poor performance of TFM in these cases which consistently oversized these defects and could not be used to estimate the defect orientation, making through-wall sizing with this method impossible.**

***Index Terms*—Super Resolution, Phased Array Imaging, Rough Cracks, Crack Sizing.**

I. Introduction

In the verification of the structural integrity of safety-critical components in the nuclear power industry, there is a drive to detect and size increasingly smaller defects. The benefits of this are centred on component safety and cost; by justifying a larger proportion of the component as defect-free, component life predictions can be lengthened and the time interval between component inspections can be extended. Ultrasonic Non-Destructive Evaluation (NDE) plays a vital role in achieving this goal and significant research has been directed towards the application of ultrasonic array imaging [1]. One important step forward to enhance ultrasonic imaging is the use of array Full Matrix Capture (FMC) [2], where all the different send-receive combinations between individual elements within the array are acquired. After a FMC data set has been collected, various imaging algorithms can be executed upon it in post-processing. A widely applied imaging algorithm to process FMC data is the Total Focussing Method (TFM) [1], [2]. Although TFM has been shown to be an accurate and robust method in a number of cases [2], [3], it is naturally restricted by the diffraction limit and therefore cannot achieve a higher resolution than half the ultrasonic wavelength. The ultrasonic wavelength is set by the inspection frequency, which in an ideal scenario would be set to the highest possible value to maximise the imaging resolution. However, the frequency cannot be indefinitely increased as undesirable effects such as material noise also increase with ultrasonic frequency and a compromise must be reached to balance resolution and minimising these unwanted effects.

Several approaches to analysing FMC data have been developed over recent years and they have demonstrated a capability to achieve a resolution beyond the diffraction limit, i.e. to achieve Super Resolution (SR). A group of these algorithms, called sampling methods, are non-iterative methods to tackle the inverse scattering problem in an attempt to approximate the profile of a scattering defect [4]–[7]. Two such algorithms are the Factorisation Method (FM) and the Time Reversal Multiple Signal Classification (TR-MUSIC) algorithm. Each works by determining whether an imaging pixel point corresponds to a location within the boundary of the scatterer by comparing the scattered field to a specified criterion. The SR capability of these algorithms has been demonstrated in NDE scenarios previously for a limited set of simple defects [8], [9] and more recently with some examples of their use in conjunction with limited aperture linear arrays [10]–[13]. It has been shown that these SR algorithms can be more sensitive to a range of factors, such as signal noise and array configuration, compared to conventional methods such as TFM [14]. This means that some of the commonly encountered industry inspection geometries and challenges may potentially restrict the wider application of SR.

One prominent challenge present within the nuclear industry is the inspection of rough embedded defects. Due to the often extreme conditions components are exposed to within this sector, defect growth mechanisms such as thermal fatigue cracking [15] and stress corrosion cracking can occur which are known to produce defects with significant surface roughness [16], [17]. Ultrasonically, the extent of defect roughness can

J. B. Elliott, M. J. S. Lowe and P. Huthwaite are with Department of Mechanical Engineering, Imperial College London, Exhibition Road, South Kensington, London SW7 2AZ, United Kingdom.

J. B. Elliott, R. Phillips and D. J. Duxbury are with Rolls-Royce Nuclear, PO BOX 2000, Derby DE21 7XX, United Kingdom. Email: josh.elliott@rolls-royce.com (J. B. Elliott).

Manuscript submitted for review February 2019.

have a major impact on the scattered field emitted from them [18], [19], often hindering their detection and characterisation which can lead to a large degree of conservatism to be placed on their inspection. This inevitably is costly to industry.

Although there is a demand within industry in general to size smaller defects which may exist within the sub-wavelength regime, an issue which could potentially be addressed by the SR algorithms, these methods must first demonstrate a significant performance enhancement compared to historically preferred techniques whilst displaying robustness to various experimental factors. Defect roughness is one such factor which must be considered before these advanced algorithms can be deployed.

This paper investigates the application of the FM and TR-MUSIC imaging algorithms in characterising rough embedded planar defects, whilst comparing their performance to conventional TFM. Given the variations encountered in defect size, orientation and roughness within NDE inspections, this investigation aims to provide a comprehensive assessment of the behaviour of the selected SR algorithms as all these defect parameters are varied. This study utilised numerical Finite Element (FE) simulations to model the array inspection of rough embedded defects, in a Monte Carlo set-up, to collect simulated FMC data sets. For each FMC data set, the FM, TR-MUSIC and the TFM imaging algorithms were applied.

The remainder of the paper is organised as follows. Firstly in Section II, a statistical description of rough cracks is introduced and the TFM, FM and TR-MUSIC algorithms are outlined. In Section III, the numerical modelling techniques that were utilised are detailed. In Section IV, the Monte Carlo study results for the series of different rough embedded planar defects are presented with a focus on assessing the imaging algorithms' characterisation capabilities. Section V discusses the main results and Section VI concludes with the key findings and suggestions for further research.

II. Background Theory

A. Model for a rough surface

A statistical framework to model rough cracks, which is commonly adopted in literature [20], is that of a Gaussian distribution of the geometric features of the rough surface; this approach was also utilised in this study. Planar 2D rough defects can be modelled simply as follows.

If the crack length is aligned along the x-axis, and the height in the y-axis, the variation of crack height, h, defined as the deviation from a flat reference surface is given by:

$$y = h(x). \tag{1}$$

The ensemble average, $\langle\ \rangle$, of the height function of the crack is assumed to be [21]:

$$\langle h \rangle = 0. \tag{2}$$

The probability density function $p(h)$ describes the probability that the surface height, h, exists between the values h and $h + dh$, where $dh > 0$. Applying Gaussian statistics, $p(h)$ can be written as [21]:

$$p(h) = \frac{1}{\sigma\sqrt{2\pi}} \exp\left(\frac{-h^2}{2\sigma^2}\right), \tag{3}$$

where σ is defined as the surface Root-Mean-Squared (RMS) height:

$$\sigma = \sqrt{\langle h \rangle} = \sqrt{\frac{1}{N\sum_{i=1}^{N} h_i^2}}. \tag{4}$$

The correlation function, $C(R)$, describes the lateral variation of the surface height by relating the height of two points along x separated by a distance R. It can be defined as [20]:

$$C(R) = \frac{\langle h(x)h(x+R)\rangle}{\sigma^2} = \exp\left(\frac{-R^2}{\lambda_0^2}\right), \tag{5}$$

where λ_0 is called the surface correlation length and is defined as the distance over which $C(R)$ decays by $\frac{1}{e}$.

Rough defect profiles were generated by using a moving average approach with the above Gaussian statistics, in line with previous studies [22], [23]. To simulate defect opening, an additional step was implemented which was to open apart two identical rough surfaces by symmetrically displacing the top and bottom surfaces by a half-cycle sinusoidal function. The maximum opening was twice the FE element size (0.1 mm) at the centre of the defect and no opening at the defect tips. This process to generate the 2D open rough cracks is shown graphically in Fig. 1. Open defects were used instead of defects with no thickness as they would more closely represent defects encountered in the nuclear sector.

Smooth defects were also created as reference imaging examples. In these cases, the defects were opened in the same way as described above but with no roughness imposed.

B. Total Focussing Method

The Total Focussing Method (TFM), as implemented in this paper, is an imaging approach which utilises FMC data [1], [2] by, in post-processing, simulating the focussing of the ultrasonic beam at predetermined nodes within a grid placed within the region of interest [3], as shown in Fig. 2. This is done by considering the times of flight from the transmitting transducer element to the grid point and back to the receiving element, and then calculating the image intensity. Referring to Fig. 2, the times of flight from transducer i to the grid point P, T_{iP} , and from point P to transducer j, T_{Pj}, are expressed as:

$$T_{iP} = \frac{\sqrt{(x_i - x)^2 + (z_i - z)^2}}{c}, \tag{6}$$

$$T_{Pj} = \frac{\sqrt{(x_j - x)^2 + (z_j - z)^2}}{c}, \tag{7}$$

where c is the wave speed. From this, the intensity of the TFM image, $I_{TFM}(P)$, for every grid point $P(x, z)$ produced by

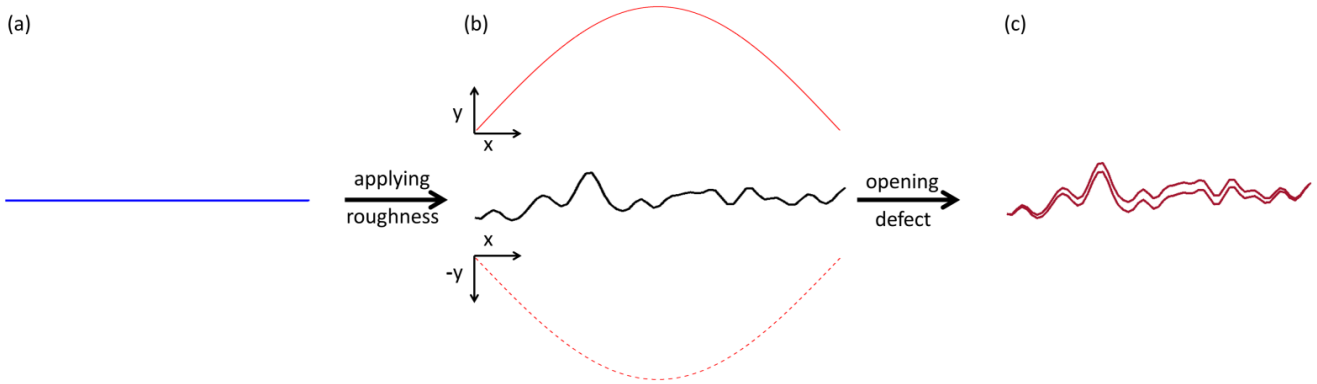

Fig. 1. Visualisation of the process to generate the 2D rough embedded defects. First a smooth defect profile is calculated (a), then roughness is applied to this profile following Gaussian statistics (b). The crack is then opened by a small amount, varying along its length, by displacing the top surface upwards by the half-cycle sinusoidal profile function shown in the solid red line at the top of (b) and similarly moving the bottom surface down by the dashed red at the bottom of (b). The resulting open 2D rough defect is shown in (c).

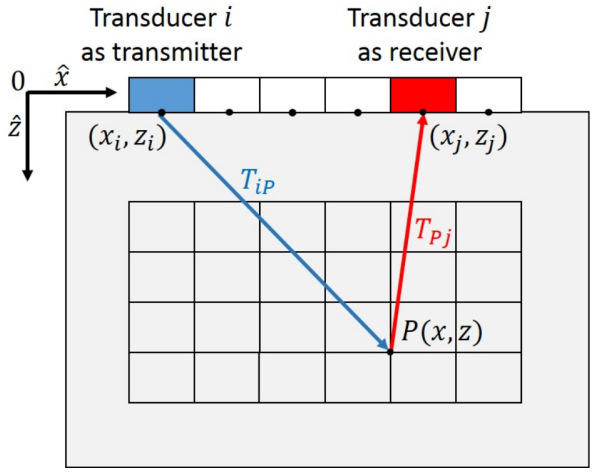

Fig. 2. The configuration of the TFM algorithm for a linear ultrasonic array.

an array of N elements is given by [2]:

$$I_{TFM}(P) = |\sum_{i,j=1}^{N} H(S_{ij})(T_{iP} + T_{Pj})| = |\sum_{i,j=1}^{N} H(S_{ij})\frac{1}{c}(\sqrt{(x_i - x)^2 + z^2} + \sqrt{(x_j - x)^2 + z^2})|, \quad (8)$$

where S_{ij} is the collected time-domain FMC signal in matrix form where transducer i is the transmitter and transducer j is the receiver, H is the Hilbert transform and $z_i = z_j = 0$.

TFM has been shown to achieve a better resolution than other array imaging methods such as focussed B-scans [2] and the imaging area of TFM can be much larger than other scanning methodologies as it utilises FMC data which is not limited to a single beam direction. This method however, along with most conventional techniques, is still diffraction limited in its resolution.

C. SR imaging algorithms

The two SR algorithms being investigated in this paper are the FM and TR-MUSIC [8], [24], [25], which both utilise FMC time domain data sets. Both of these algorithms start by converting FMC data captured by ultrasonic arrays into the frequency domain, ω, as part of the process to generate the multistatic response matrix $K(\omega)$ [24]. From this matrix, singular value decomposition (SVD) can be conducted to generate a set of singular eigenvalues, μ_i, and their corresponding eigenvectors, ν_i, where $i = 1, 2, ..., N$ and N corresponds to the number of elements in the ultrasonic array.

In this study where the FM has been utilised, all eigenvectors generated from the SVD of the K matrix were considered whereas in the application of the TR-MUSIC algorithm, the eigenvectors were separated into two separate subspaces; the signal subspace and the noise subspace. In an idealised noise free scenario, there would exist a set of non-zero eigenvalues whose corresponding eigenvectors belong to the 'signal' subspace and the remaining eigenvectors would belong to the 'noise' subspace. In practice, there exists a finite level of noise in the inspection system so a non-zero threshold value must be used to determine the point of separation between these two subspaces and the separation point varies depending on the particular inspection case. The typical threshold values used in this work were around 30 dB less than the maximum eigenvalue calculated, based on observing a step function-like separation in amplitude between the signal and noise subspace eigenvalues. Although there have been some cases presented within the literature of also separating eigenvalues in the application of the FM, the majority utilise the full eigenvalue range thus the results presented in this study aimed to compare the most common implementation of these algorithms.

A key part of both the SR imaging algorithms is their use of the steering vector, g, to propagate the eigenvectors to different positions, $\mathbf{r}$, in the imaging grid:

$$g(\mathbf{r}) = [G(\mathbf{R}_1, \mathbf{r}), G(\mathbf{R}_2, \mathbf{r}), ..., G(\mathbf{R}_N, \mathbf{r})], \quad (9)$$

where $\mathbf{R}_N$ corresponds to the N array element locations and G correspond to the Green's function of the propagation medium.

The image pseudospectrum for the TR-MUSIC, I_{TRM}, is given by [25]:

$$I_{TRM}(\mathbf{r}) = \frac{1}{\sum_{j=M+1}^{N} |\langle g(\mathbf{r})|\nu_j\rangle|^2}, \quad (10)$$

where $\langle \ | \ \rangle$ refers to the bra-ket notation, and M is fewer than the number of transducers N. This algorithm only considered the eigenvectors with the largest eigenvalues corresponding to the 'signal' subspace. In this study, the value of M corresponded to the number of eigenvalues below the cut-off threshold applied as mentioned above (30 dB). Typically $M > 55$, leaving around 8 significant eigenvectors. The value of M remained relatively stable even in the presence of defect roughness.

The image pseudospectrum for the FM, I_{FM}, is given by [8]:

$$I_{FM}(\mathbf{r}) = \frac{1}{\sum_{j=1}^{N} \frac{1}{|\mu_j|} |\langle g(\mathbf{r})|\nu_j\rangle|^2}. \quad (11)$$

The algorithms essentially work by determining the likelihood that a point scatterer exists at the imaging grid points, based on the scattered field information. Hence when imaging small planar defects, strong indications are often produced from the tips of the defects as the diffraction effects from these locations correspond most closely to that of point scatterers. It is from these tip locations that the defect length and orientation can be estimated. This sizing methodology is often not possible with TFM images of small defects and amplitude based methods must be applied. For volumetric defects, such as large pores and side drilled holes, similar indications are produced from the SR algorithms as when applied to planar defects. However, as the defect size approaches zero and becomes more point-like, only single indications are produced by the algorithms and no direct sizing information can be gained. In these cases, one could infer that the defect size is smaller than the smallest defect size that can be reliably characterised.

The above SR algorithms were modified to utilise K matrix data over a range of frequencies, the resultant multiple frequency factorisation method (MF-FM) and multiple frequency TR-MUSIC (MF-TR-MUSIC) algorithms being shown below [26]:

$$I_{MF-TRM}(\mathbf{r}) = \frac{1}{\sum_{\omega} \sum_{j=M+1}^{N} |\langle g(\mathbf{r},\omega)|\nu_j(\omega)\rangle|^2}, \quad (12)$$

$$I_{MF-FM}(\mathbf{r}) = \frac{1}{\sum_{\omega} \sum_{j=1}^{N} \frac{1}{|\mu_j|} |\langle g(\mathbf{r},\omega)|\nu_j(\omega)\rangle|^2}. \quad (13)$$

It was found that the multiple frequency SR algorithms demonstrated a higher robustness to defect roughness, and therefore they were chosen to be used in this study. In addition, by using a range of frequencies, the imaging performance became less reliant on accurately selecting a single specific frequency value corresponding to the centre frequency of the ultrasonic signal, which allowed easier automation of applying the SR methods to the FMC data sets. In this study, a 2 MHz input ultrasonic toneburst was used and the frequency range for the SR algorithms was set to 0.4 MHz. This was approximately the full width at half maximum of the bandwidth profile of the ultrasonic toneburst. A total of 9 equally spaced frequency values were sampled across this frequency range when implementing the MF-FM and MF-TR-MUSIC methods. All SR images and results discussed subsequently in this paper refer to the application of the MF-FM and MF-TR-MUSIC algorithms.

III. Methodology

A. Simulation set up

To model an array inspection of 2D rough planar defects, full Finite Element (FE) simulations were used with a separate model containing each rough defect realisation in the Monte Carlo study. The simulations were run using the GPU-based solver Pogo [27], which allowed significantly faster simulation run times compared to conventional CPU-based FE solvers.

The inspection schematic used for the FE models is shown in Fig. 3. In all cases, a steel block was simulated with dimensions of 100 mm x 50 mm. The 64-element 2 MHz array was modelled using a series of pure longitudinal wave point sources at the array element positions, which were separated by half the ultrasonic longitudinal wave wavelength corresponding to the centre frequency ($\frac{\lambda}{2}$=1.5 mm). This separation is typical of ultrasonic arrays. On reception of the ultrasonic signal, only the component of displacement normal to the array length was recorded. To model the longitudinal wave point sources, the closest four nodes within the FE mesh located about the excitation positions, corresponding to the phased array element centre points, were exited uniformly radially away from those location. This ensured that symmetric radially emanating longitudinal waves were generated, with a shear wave component close to zero.

The steel block region in the FE models were surrounded by regions of Absorbing Layers with Increased Damping (ALIDs) [28], [29]. These layers were used to absorb unwanted reflections from model boundaries to help ensure that only the defect scattered signal was recorded by the array. The FE element size, d, was set to 50 μm which corresponds to $\frac{\lambda}{d}$=60. It was set to this value to best conform to the rough surfaces being generated so as to capture as much of the complex scattering as possible. Previous work has shown this level of refinement to be sufficient for these types of surfaces [22], [30]. The ALIDs were set to be 180 FE elements thick (3λ). The FE meshes consisted of triangular elements and were structured everywhere, except in the local region of the defect where they were set to be irregular to allow for optimal conformity to the defect profile.

A case with no defect was modelled to capture any small unwanted reflection from the ALIDs and this recorded FMC data was subtracted from all subsequent defect simulations.

The defects were centred symmetrically under the array to maximise the viewing angle on the defects to enhance the SR imaging capability, at a depth of 42 mm (14λ) from the array. The work presented in this study considered idealised cases where the ultrasonic array viewing angle has been maximised for a particular inspection scenario and the imaging algorithms were applied to noise-free FE simulation data. It should be noted that both noise and viewing angle can have significant

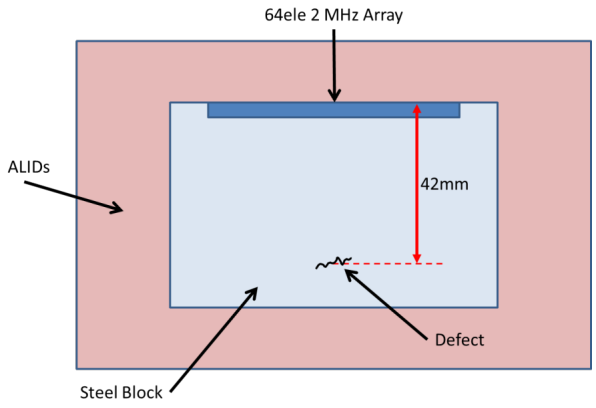

Fig. 3. The FE inspection set-up for the array imaging of 2D rough defects. The origin position of the models is located at the centre of the defect.

TABLE I
The rough defect cases investigated in this study, each with their corresponding parameters. 0° inclination angle was defined to be parallel to the ultrasonic array.

Defect Length (mm)	Inclination Angle (°)	σ (μm)	λ_0 (μm)
1.5	0	10	150
1.5	45	10	150
1.5	0	100	150
1.5	45	100	150
3	0	10	150
3	45	10	150
3	0	100	150
3	45	100	150

effects on the performance of SR imaging. The impact of these parameters on imaging have been studied elsewhere (see [[11], [14]]) and therefore have not been evaluated further here.

B. Rough defect inspection cases

A series of rough defect cases with different parameters were used in this study and are listed in Table I. The values of σ and λ_0 were chosen in line with typical experimentally measured values from thermal fatigue and stress corrosion cracks from components within the nuclear industry [16], [17]. Although the defect growth mechanism and component material can lead to large variations in the resultant defect parameters, it was reported that thermal fatigue cracking produced defects with $\sigma \approx 10-20$ μm and $\lambda_0 \approx 100-200$ μm in ferritic low alloy steels and $\sigma \approx 70-100$ μm and $\lambda_0 \approx 100-200$ μm in stainless steels [16], [17]. Stress corrosion cracking defects were shown to exhibit roughly the same parameters. These types of defects were considered to be the most relevant to the potential application of array inspections utilising SR algorithms, hence rough defects with $\lambda_0 = 150$ μm and $\sigma = 10$ μm, 100 μm were considered.

For each defect length, roughness and orientation combination listed in Table I, 100 different FE realisations were used when assessing the imaging algorithms' performances. To justify the total number of realisations, the statistical variation of the measured length for each rough defect parameter set was calculated and the results showed good convergence with only slight variations remaining for some of the higher roughness cases. This provided a basis to legitimise any results derived from the Monte Carlo study. This number of realisations to achieve adequate convergence is also consistent with the results presented by Pettit *et al.* [22]. Defect lengths of 1.5 mm ($\frac{\lambda}{2}$) and 3 mm (λ) were considered to focus the investigation on small defects at or below the ultrasonic wavelength. Defect inclinations of 0° and 45° were selected to compare the performance differential between an optimal defect orientation (0°) to a non-optimal case.

In addition, a smooth defect case was run for each combination of defect length and inclination angle shown in Table I to establish a benchmark for the different algorithms.

C. Defect sizing methodologies

When using conventional TFM, a 6 dB box fitting algorithm was applied to the images to provide an estimate of the size and orientation of the defect in cases where tip diffraction signals could not be resolved. This sizing algorithm fitted a parallelogram box to the TFM images with the constraint that the box must contain all image pixels within a -6 dB range of the maximum crack pixel value. The algorithm finds the optimal orientation of the box such that all the pixels above -6 dB are included whilst minimising the number of pixels which are below this threshold. The defect length was attributed to the length of the pair of parallelogram sides orientated in the direction closest to the known defect orientation. The slant angle of this same pair of sides was the measured defect inclination. In the cases where crack tip indications could be resolved, the centres of the tip indications were identified and a straight line was joined between them, from which the length and orientation was calculated.

As mentioned in Sec. II-C, the SR algorithms' theory assumes point scatterers and thus returns strong indications from the tips of defects. As with some of the TFM images, the centres of these SR tip indications were identified and the same method of assuming the defect profile was the straight line between them was used to estimate the defect length and orientation. In every SR imaging instance, the tip indications could be resolved and therefore the SR algorithms exclusively used this sizing technique. To ensure that only the first longitudinal defect scattered signal was used when implementing the SR algorithms, time domain processing was applied to the FMC data sets. This was achieved by windowing the time traces with a Hann window at the appropriate temporal location. As the defect location was known in each simulation case, knowing where to implement the window was trivial. In a realistic case where the defect location is not known, it is suggested that TFM is applied to gauge the approximate defect location before subsequently using this information to conduct the windowing prior to applying the SR methods.

IV. Results

For each of the rough defect realisations and smooth defect cases, the TFM, MF-FM and MF-TR-MUSIC algorithms were applied to the simulated FMC data sets and the sizing methodologies described in Sec. III-C were implemented to estimate the defect length and orientation from the images. The pixel size in all image reconstructions was set to 50 μm.

A. Smooth defects

It is important to assess the performance of the SR algorithms on smooth defects initially before adding further complexities to the inspection, such as defect roughness, in order to establish their baseline capabilities. The images produced for these smooth defect cases are shown in Fig. 4 and the associated characterisation results are detailed in Table II.

First considering the 1.5 mm ($\frac{\lambda}{2}$) smooth defect results in Table II, it can be seen that the MF-FM and MF-TR-MUSIC algorithms produce far more accurate results than TFM for both inclination values. There is a 1-2% error in the length sizing of the SR algorithms for both orientations, compared to the 13-30% overestimation of TFM. In terms of estimating the defect inclination, TFM produces the same estimation of 0° for both defect orientations indicating that the technique is not viable to measure this parameter for defects on this scale. This is visible in the images in Fig. 4(c) and (f) where the limited resolution of TFM of half a wavelength, equal to the crack length, results in a single blurred indication and gives no measure of orientation. The SR algorithms are not limited in this way and they estimate the defect angles successfully to within 2° and 7° in the 0° and 45° cases respectively. This in turn allows good estimation of defect through-wall heights (TWHs); this is the projection of the defect size in the component thickness direction and hence depends on angle.

Considering the 3 mm (λ) 0° smooth defect imaging results in Table II, TFM now performs with excellent accuracy as it is no longer diffraction limited. The SR algorithms still perform well with around a 4% error in sizing and less than 1° error in inclination estimation. In the 3 mm 45° case however, there is a significant drop-off in performance for all the algorithms. TFM is able to resolve the tip diffraction signals, however it undersizes the length by around 20% despite accurately estimating the inclination. Both of the SR algorithms oversize the defect significantly, with the MF-FM overestimating the length by 23% and the MF-TR-MUSIC algorithm by 46%. This is visible in the images in Fig. 4(j) and (k) where the defect tip indications can be seen to deviate from the actual tip location considerably.

B. Rough defects

To begin the analysis beyond the smooth cases, the 1.5 mm ($\frac{\lambda}{2}$) 0° rough defect imaging results were considered. Representative images from the imaging algorithms produced for the 1.5 mm defects, with each of the orientation and roughness combinations, are shown in Fig. 5. In total, 100 separate FE realisations were run for each defect parameter combination shown in Fig. 5, from which the statistical mean and standard deviation of the defect length and inclination angle were calculated to determine the performance of each algorithm. The standard deviation was used as the statistical error for the obtained results.

Fig. 6 compares the sizing and orientation estimation results of all the algorithms to the true values for the 1.5 mm 0° 10 μmm and 100 μmm rough defect cases. It can be seen that in the 10 μm cases, both of the SR algorithms estimate the defect length more accurately than TFM. Both of the SR algorithms' mean length estimations are within one standard deviation of the true value of 1.5 mm, with MF-FM producing a result of (1.47$\pm$0.04) mm and the MF-TR-MUSIC estimating the length to be (1.490$\pm$0.015) mm. TFM overestimates the defect length, (1.701$\pm$0.004) mm, due to the blurring caused by the resolution limit. In terms of estimating the defect inclination, MF-TR-MUSIC is accurate with a small standard deviation. MF-FM has a slight negative bias in its inclination estimation and the mean value is just over one standard deviation from the true value of 0°. The value it estimates is still close to the true value and is accurate enough to have negligible influence on correctly estimating the through-wall height of the defect. TFM is accurate in its estimation of the 0° inclination, however, as has been shown from the smooth cases, this is a misleading result as it cannot estimate this parameter for small defects. Comparing these results to the smooth defect results, it is clear that the effect of low roughness was negligible on the imaging capability of the algorithms.

Now comparing the 10 μm results to the 100 μm results in Fig. 6, the most apparent difference is the increased standard deviation in the SR algorithms' inclination estimations, with both methods having a standard deviation of 20° compared to less than 5° previously. This was attributed to how the positions of the 100 μm rough tip ends generally exhibited had significant vertical variation compared to the 10 μm cases. This is shown in Fig. 5 where in the images (a) and (b), the rough crack tips lie in approximately the same depth plane and therefore so do the SR indications. However in plots (d) and (e), the rough crack tips do not lie in the same depth plane and thus neither do the SR indications, inevitably outputting non-zero inclination estimations. TFM in this case again misleadingly produced inclination estimations close to the correct value of 0°, a result of its inability to estimate this parameter for the $\frac{\lambda}{2}$ sized defects. Importantly, the SR algorithms still produced more accurate length estimations compared to TFM despite the increased roughness. The estimations produced were (1.52$\pm$0.045) mm for MF-TR-MUSIC and (1.43$\pm$0.05) mm for MF-FM, which are more accurate than the (1.78$\pm$0.035) mm for TFM.

The averaged characterisation results for the 1.5 mm 45° rough defects are shown in Fig. 7. As can be seen in the low 10 μm roughness results, both of the SR result algorithms outperform TFM in estimating the defect length and inclination. MF-FM estimated these parameters to be (1.46$\pm$0.04) mm and (39$\pm$2)$^\circ$, MF-TR-MUSIC estimated them to be (1.44$\pm$0.02) mm and (38$\pm$1)$^\circ$ and TFM estimated them to be (1.96$\pm$0.02) mm and (1$\pm$1.5)$^\circ$. TFM again shows its limited performance when imaging sub-wavelength defects

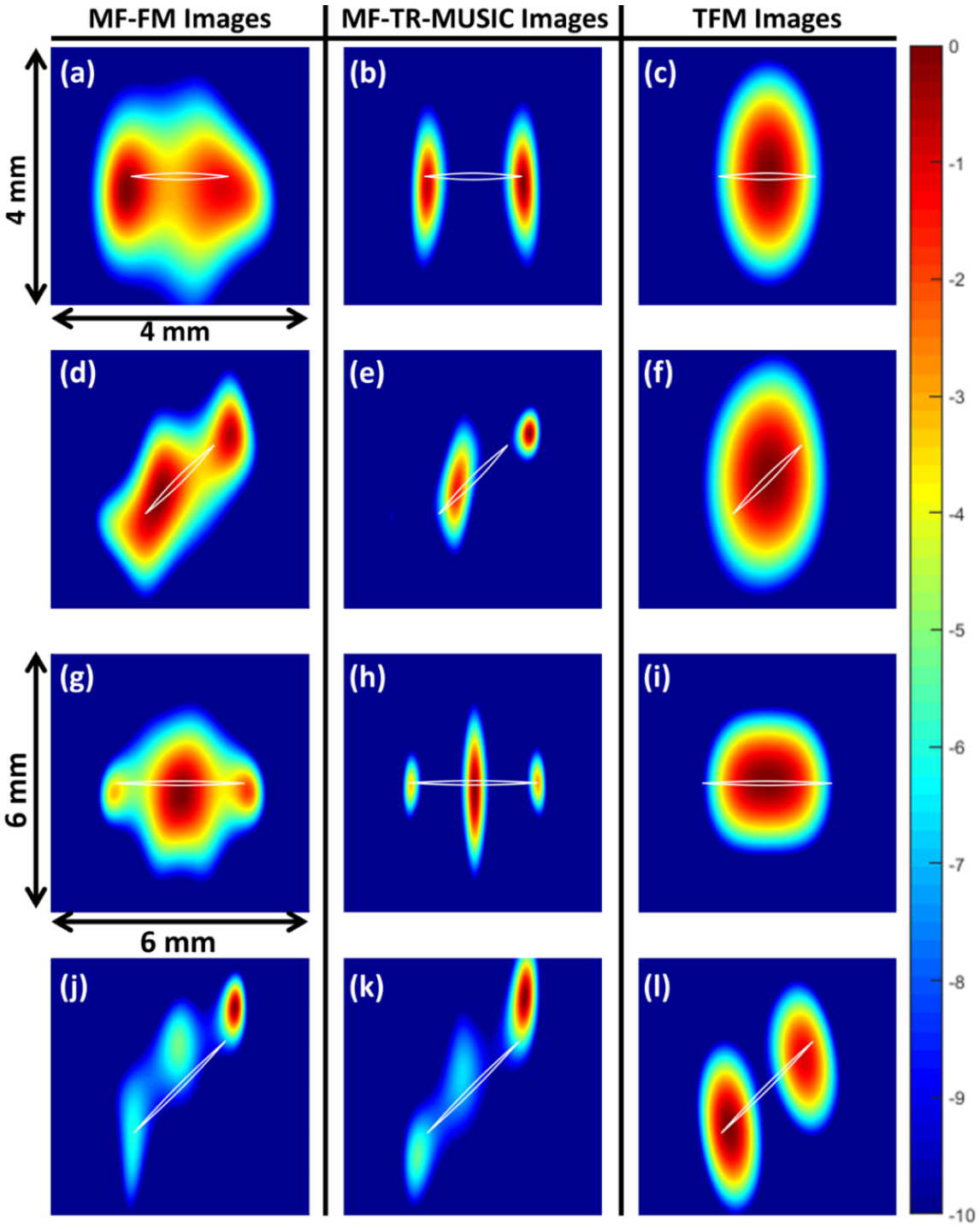

Fig. 4. Images from the MF-FM, MF-TR-MUSIC and TFM algorithms for the smooth defect cases. Images a), b) and c) correspond to 1.5 mm 0° defects; d), e), and f) correspond to 1.5 mm 45° defects; g), h) and i) correspond to 3 mm 0° defects; j), k) and l) correspond to 3 mm 45° defects. All the images are plotted on a decibel scale normalised to the maximum image amplitude from the defect response. Images (a)-(f) are 4 mm x 4 mm in size, images (g)-(l) are 6 mm x 6 mm in size.

as it provides poor estimations for defect length as well as not being able to estimate the defect inclination at all. For the 1.5 mm 45° 100 μm roughness results, the same trends as for the low roughness cases are observed. Despite reduced performance with the higher roughness, both SR algorithms were significantly more accurate than TFM in estimating the defect parameters, with around 25% better length sizing accuracy and 50% better orientation estimation. MF-FM estimated the defect parameters to be (1.54±0.05) mm and (33±5)°, MF-TR-MUSIC estimated them to be (1.64±0.1) mm and (40±5)° and TFM estimated them to be (1.92±0.15) mm and (13±10)°.

Representative images from the imaging algorithms for the 3 mm (λ) defects with each of the orientation and roughness

TABLE II
The average characterisation results for all smooth defect equivalent cases when applying all algorithms.

Actual			**MF-FM**			**MF-TR-MUSIC**			**TFM**		
Size (mm)	Size (λ)	Angle (°)	Length (mm)	Length Error (%)	Angle (°)	Length (mm)	Length Error (%)	Angle (°)	Length (mm)	Length Error (%)	Angle (°)
1.5	0.5	0	1.51	0.7	1.91	1.51	0.7	1.91	1.7	13.3	0
1.5	0.5	45	1.46	-2.5	40.84	1.47	-2.0	38.07	1.95	30	0.001
3	1	0	3.12	5	0.92	2.92	2.7	0.99	3	0	0
3	1	45	3.70	23.4	46.13	4.37	45.7	54.87	2.35	-21.7	43.29

combinations are shown in Fig. 8. The same analysis as for the 1.5 mm rough defect results were applied and the averaged characterisation parameters from the algorithms are plotted in Fig. 9 and Fig. 10, corresponding to the 0° and 45° inclined cases respectively. From the 3 mm 0° averaged results shown in Fig. 9, it can be seen that in both roughness cases, despite the SR algorithms being able to estimate the defect length and inclination relatively accurately, they are not as accurate as TFM which is now operating well within its resolution capability. This performance differential is most apparent in the 10 μm case where TFM is extremely accurate in terms of estimating the defect length and inclination.

Considering the 3 mm 45° results presented in Fig. 10, it is observed that there is a contrast in the performance of the SR algorithms between the different roughness cases. In the low roughness 10 μm case, the averaged results are similar to the smooth defect results presented in Table II, with both SR algorithms overestimating the defect parameters significantly and TFM producing comparatively more accurate results. The difference comes when considering the higher roughness 100 μm case where the length sizing accuracy of both SR algorithms increases dramatically to within 10% error, which makes them slightly better than TFM. This increase in performance can be visually seen by comparing the images shown in Fig. 8(g) and (h) to the images in Fig. 8(j) and (k), where in the rougher 100 μm defect cases, the SR algorithms produce tip indications much closer to the actual defect tip locations than in the 10 μm defect cases.

The quantitative characterisation results discussed above are summarised in Table III, Table IV and Table V.

V. Discussion

A. Smooth defects

The results shown in Sec. IV-A demonstrate that the SR algorithms could provide an accurate sizing capability for sub-wavelength smooth defects. These SR results significantly outperformed TFM for defects on this size scale which tended to overestimate the defect length by around 15%, compared to the small SR error of around 2%. The SR algorithms additionally showed good defect orientation estimation performance for both 0° and 45° cases, unlike TFM which could not estimate this parameter effectively. This is a significant result as it demonstrates that through-wall sizing is achievable using the SR algorithms on $\frac{\lambda}{2}$ sized smooth inclined planar defects. The TWH of defects is a vital parameter that must be estimated accurately in most inspections as it often can be the largest influence on the structural integrity of components. The lack of performance of TFM was attributed to the defect length being at the diffraction limit and it was shown that the SR algorithms could potentially bridge this performance gap on this size scale.

For larger wavelength sized defects, the results showed there was no significant benefit of applying the SR algorithms over conventional TFM as generally TFM produced accurate characterisation results comparable or slightly better than the SR methods. This was expected as these defects were comfortably within the theoretical resolution limit of the method.

B. Rough defects

The rough defect imaging results detailed in Sec. IV-B have shown there is potential for the SR algorithms to size sub-wavelength planar defects accurately even when the flaws exhibit roughness parameters representative of in-service flaws in the nuclear sector. For the $\frac{\lambda}{2}$ sized rough defects, the SR algorithms demonstrated significantly better sizing capability than TFM for roughness values up to 100 μm, with averaged results similar to the smooth defect equivalent cases. The standard deviation error associated with the sizing results for the SR algorithms in these cases were very similar to those obtained from conventional TFM meaning the performance of the various methods can be directly compared to each other. The SR algorithms also maintained capability to estimate defect orientation which it demonstrated for smooth defects meaning their TWH sizing performance is also robust to the levels of roughness considered in the study.

For the wavelength sized rough defects, similar trends to the smooth defect equivalent cases were observed where TFM produced the more accurate and precise sizing and orientation estimation results. The one exception to this trend was for the 3 mm 45° 100 μm averaged results which showed that the SR sizing performance increased dramatically from the smooth case and it outperformed TFM. It is unclear the exact origin of this result; it is suggested that it could be due to the increased scattered signal being received by the array because of the

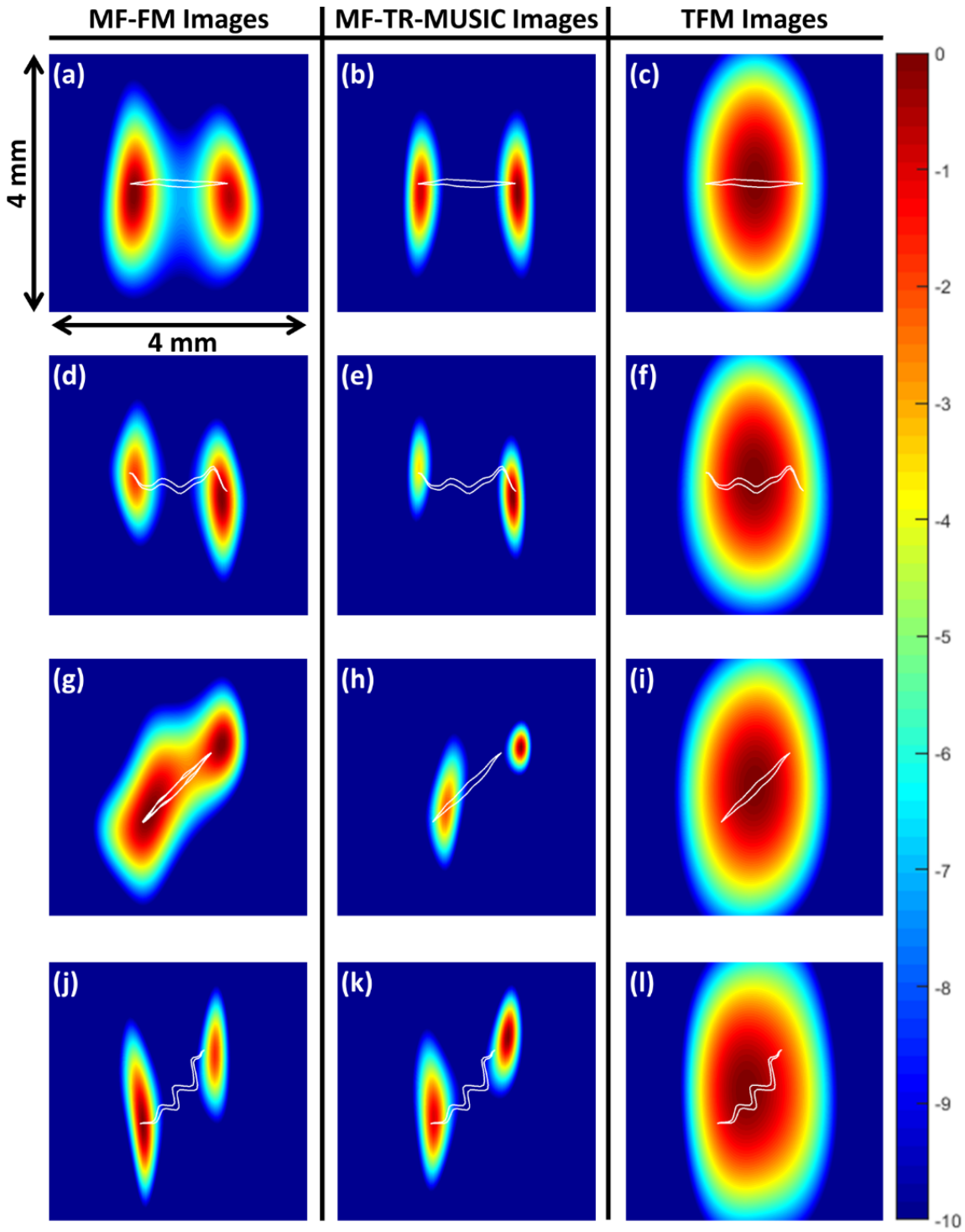

Fig. 5. Representative images from the MF-FM, MF-TR-MUSIC and TFM algorithms for 1.5 mm rough defects. Images a), b) and c) correspond to $\sigma = 10$ μm 0° rough defects; d), e), and f) correspond to $\sigma = 100$ μm 0° rough defects; g), h) and i) correspond to $\sigma = 10$ μm 45° rough defects; j), k) and l) correspond to $\sigma = 100$ μm 45° rough defects. All the images are plotted on a decibel scale normalised to the maximum image amplitude from the defect response.

increase in magnitude of the diffuse scattered field component for the rougher inclined defects. This would usually hinder conventional TFM as it could obscure the much weaker tip diffraction signals but it seemed to enhance the SR imaging performance.

Considering the potential practical deployment of the SR methods, it is recommended that it is used in conjunction with conventional methods for several reasons. Firstly, it is a requirement of the SR algorithms to process only the defect scattered signal so collected ultrasonic data must be appropriately windowed based on a priori knowledge of approximately where the defect is located in the component.

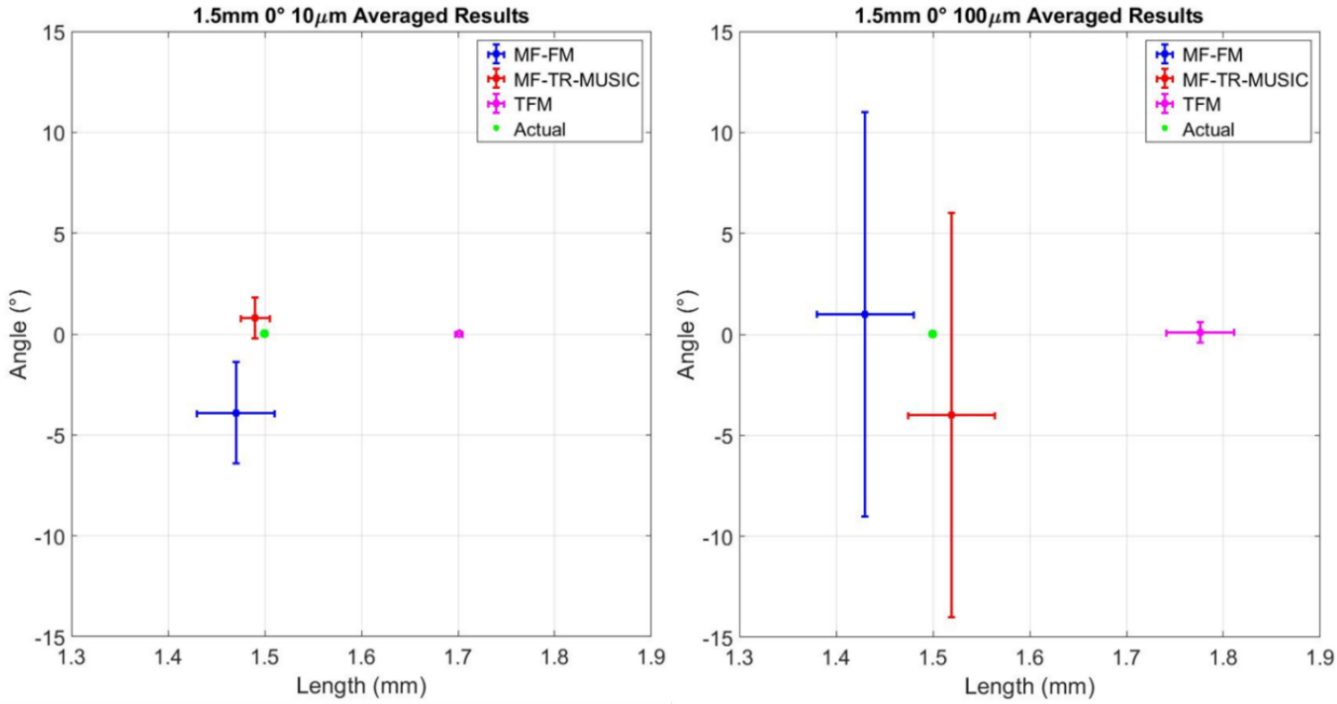

Fig. 6. The mean estimated defect length and inclination angle values calculated from the 100 realisations for the 1.5 mm 0° 10 μm (left plot) and 1.5 mm 0° 100 μm (right plot) rough defects. The error bars correspond to the standard deviation of the length and angle results.

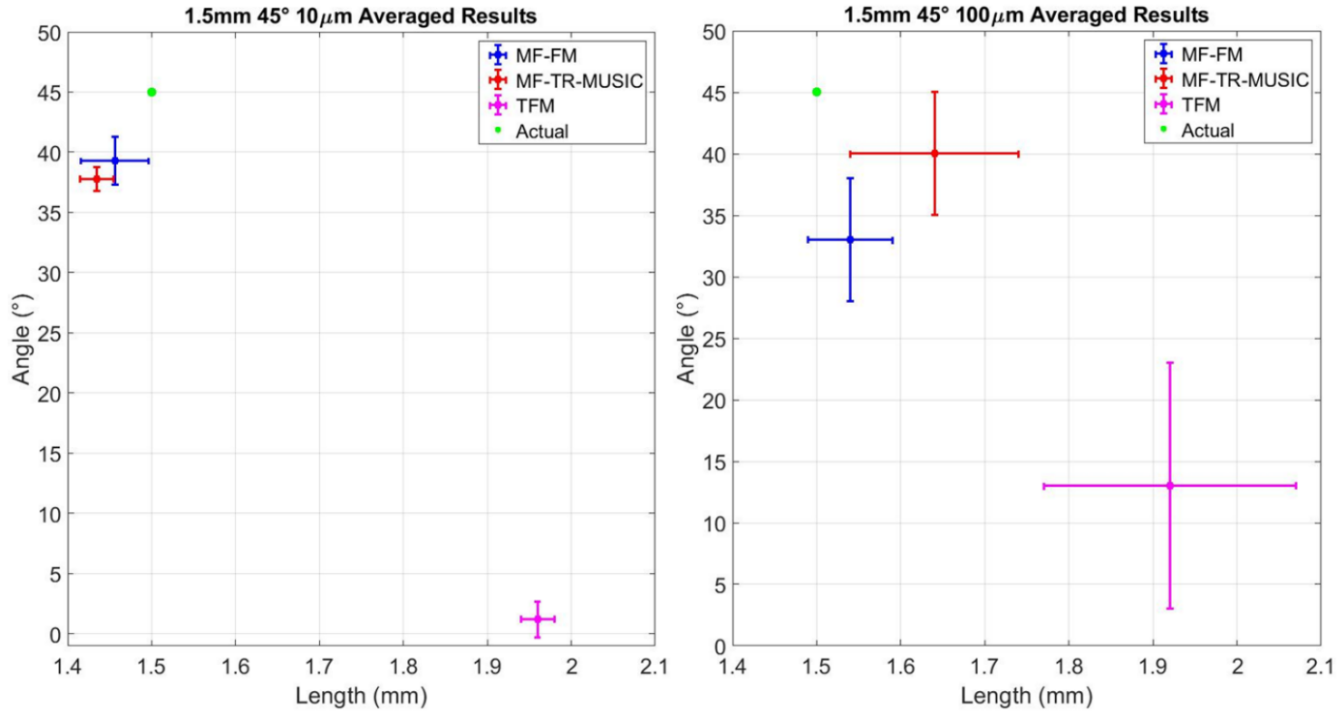

Fig. 7. The mean estimated defect length and inclination angle values calculated from the 100 realisations for the 1.5 mm 45° 10 μm (left plot) and 1.5 mm 45° 100 μm (right plot) rough defects. The error bars correspond to the standard deviation of the length and angle results.

This basic prior knowledge is suggested to be attained using simple conventional techniques or with TFM. Secondly, the SR images predominantly show strong indications from the planar defect tip locations and not a consistent surface response. This may lead to confusion in classifying the defect type from the images, i.e. whether the indications shown in Figure 5 were caused by two close-by point reflectors or a single planar flaw. Further work must be conducted to try to overcome this limitation. Nevertheless, the SR algorithms have still demonstrated a superior sizing capability compared to TFM thus even when

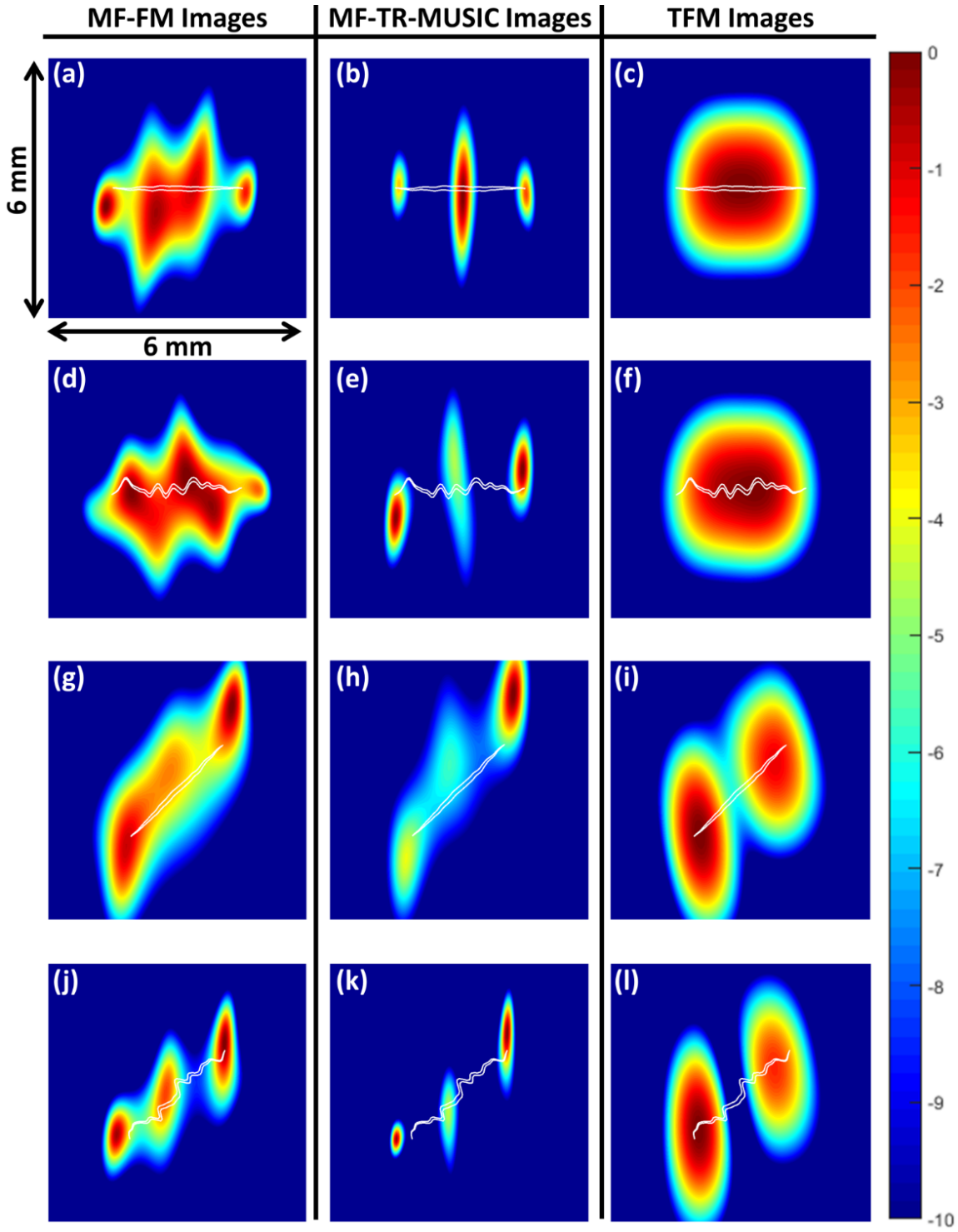

Fig. 8. Representative images from the MF-FM, MF-TR-MUSIC and TFM algorithms for 3 mm rough defects. Images a), b) and c) correspond to $\sigma = 10$ μm 0° rough defects; d), e), and f) correspond to $\sigma = 100$ μm 0° rough defects; g), h) and i) correspond to $\sigma = 10$ μm 45° rough defects; j), k), l) correspond to $\sigma = 100$ μm 45° rough defects. All the images are plotted on a decibel scale normalised to the maximum image amplitude from the defect response.

considering the worst case defect characterisation result where a small volumetric defect is classified as a small planar crack, a less pessimistic size would be obtained via the SR methods.

Due to the strict regulatory restrictions imposed upon the UK nuclear sector, advanced array imaging algorithms such as the SR methods and even TFM are not widely used as of yet. The nuclear industry currently prefers to use conventional temporal and scanning imaging techniques such as Time-Of-Flight Diffraction and simple B-scan plots. These methods, although tried and tested for many years, are intrinsically limited in several aspects. For new methods to be deployed in addition to the current methods or to replace them, they

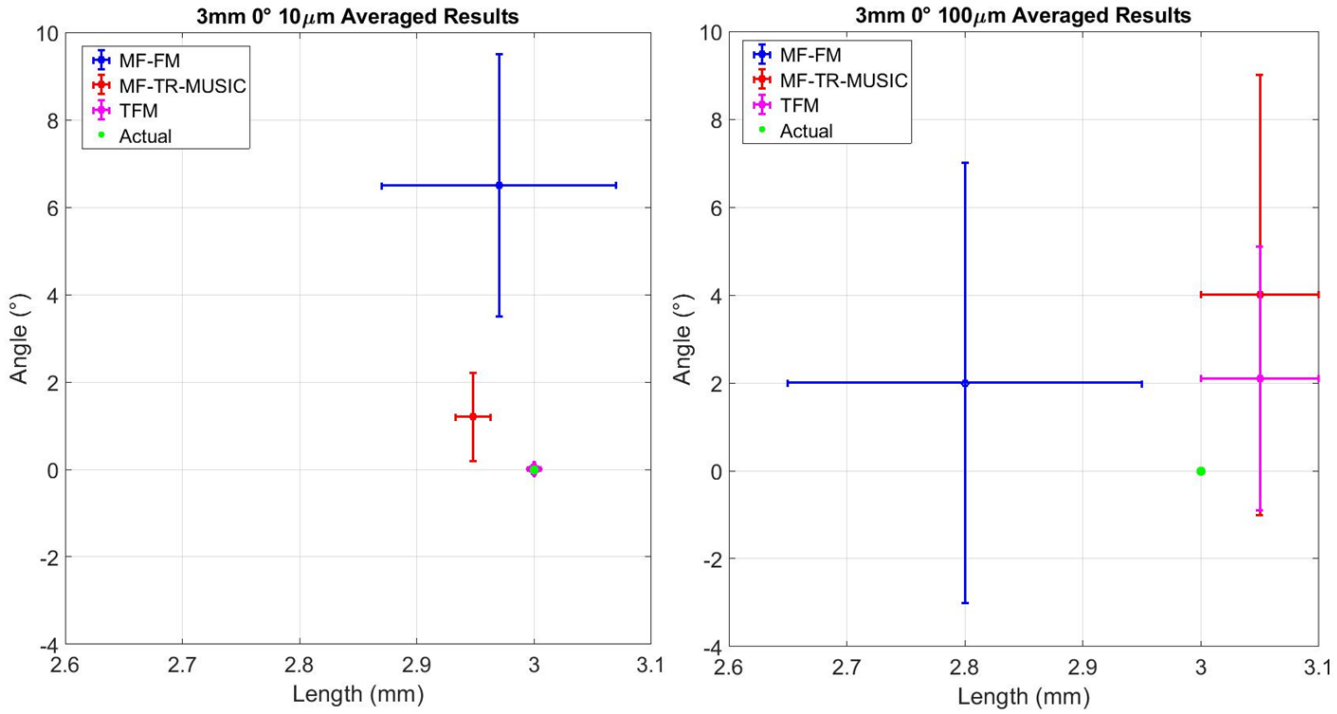

Fig. 9. The mean estimated defect length and inclination angle values calculated from the 100 realisations for the 3 mm 0° 10 μm (left plot) and 3 mm 0° 100 μm (right plot) rough defects. The error bars correspond to the standard deviation of the length and angle results.

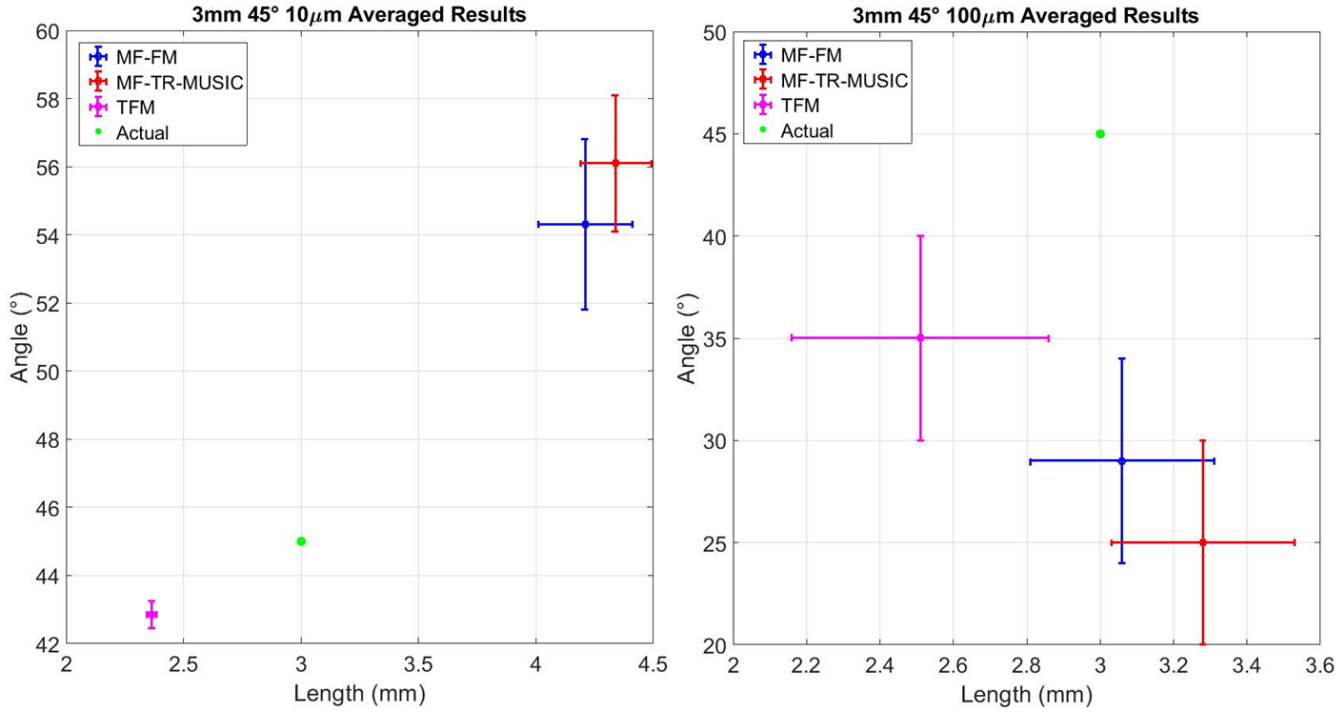

Fig. 10. The mean estimated defect length and inclination angle values calculated from the 100 realisations for the 3 mm 45° 10 μm (left plot) and 3 mm 45° 100 μm (right plot) rough defects. The error bars correspond to the standard deviation of the length and angle results.

must be stringently validated to show reliability and robustness to in-service inspection conditions. By considering the impact of defect roughness, the results presented in this study mark a step forward for validating the performance of the FM and TR-MUSIC algorithms on realistic defects. To continue down this path, further work needs to be conducted such as testing their performance on different component and defect geometries, material properties and inevitably by conducting extensive experimental trials on representative in-service test pieces.

TABLE III
The average characterisation results for all rough defect classes when applying the MF-FM algorithm. Std means standard deviation.

Actual			**Measured (MF-FM)**			
Size (mm)	Angle (°)	σ (μm)	Length (mm)	Length Std (mm)	Angle (°)	Angle Std (°)
1.5	0	10	1.47	0.08	-3.9	5
1.5	45	10	1.456	0.08	39.3	4
1.5	0	100	1.43	0.1	1	20
1.5	45	100	1.54	0.1	33.3	10
3	0	10	2.97	0.2	6.5	6
3	45	10	4.21	0.4	54.3	5
3	0	100	2.8	0.3	2	10
3	45	100	3.06	0.5	29	10

TABLE IV
The average characterisation results for all rough defect classes when applying the MF-TR-MUSIC algorithm. Std means standard deviation.

Actual			**Measured (MF-TR-MUSIC)**			
Size (mm)	Angle (°)	σ (μm)	Length (mm)	Length Std (mm)	Angle (°)	Angle Std (°)
1.5	0	10	1.49	0.03	0.8	2
1.5	45	10	1.435	0.04	37.8	2
1.5	0	100	1.519	0.09	-4	20
1.5	45	100	1.64	0.2	40	10
3	0	10	2.948	0.03	1.2	2
3	45	10	4.34	0.3	56.1	4
3	0	100	3.05	0.1	4	10
3	45	100	3.28	0.5	25	10

TABLE V
The average characterisation results for all rough defect classes when applying the TFM algorithm. Std means standard deviation.

Actual			**Measured (TFM)**			
Size (mm)	Angle (°)	σ (μm)	Length (mm)	Length Std (mm)	Angle (°)	Angle Std (°)
1.5	0	10	1.701	0.007	0.0002	0.0003
1.5	45	10	1.96	0.04	1.2	3
1.5	0	100	1.776	0.07	0.1	1
1.5	45	100	1.92	0.3	13	20
3	0	10	3	0	0.0003	0.0004
3	45	10	2.364	0.04	42.85	0.8
3	0	100	3.05	0.1	2.1	6
3	45	100	2.51	0.7	35	10

VI. Conclusion

In this paper, the FM and TR-MUSIC imaging algorithms are compared against the TFM method in the ultrasonic array inspection of 2D embedded rough planar defects. A Monte Carlo finite element simulation study was conducted for varying defect parameters including sizes, orientation and roughness parameters comparable to that of in-service defects from the nuclear sector generated by thermal fatigue and stress corrosion cracking mechanisms. The results presented show that for sub-wavelength ($\frac{\lambda}{2}$) defects, both of the SR algorithms were able to size and estimate defect orientation accurately for the smooth case and for rough defects up to $\sigma = 100\ \mu m$. This was in contrast to the poor performance of TFM in these cases which consistently oversized these defects and could not be used to estimate the defect orientation, making through-wall sizing with this method impossible. The work in this paper is a step towards the application of these imaging methods in the nuclear industry and demonstrates the potential of these algorithms in dealing with some of the challenges facing the sector today.

Acknowledgment

The funding for this work was provided by EPSRC research fellowship EP/I017704/1 for the Centre for Doctoral Training in NDE and the UK Ministry of Defence. The Royal Commission for the Exhibition of 1851 also provided a financial contribution towards this work through an Industrial Fellowship. Dr Peter Huthwaite is funded by EPSRC Early Career Fellowship EP/M020207/1.

References

[1] B. W. Drinkwater and P. D. Wilcox, "Ultrasonic arrays for non-destructive evaluation: A review", *NDT & E International*, vol. 39, no. 7, pp. 525-541, 2006.

[2] C. Holmes, B. W. Drinkwater and P. D. Wilcox, "Post-processing of the full matrix of ultrasonic transmit–receive array data for non-destructive evaluation", *NDT & E International*, vol. 38, no. 8, pp. 701-711, 2005.

[3] C. Holmes, B. W. Drinkwater and P. D. Wilcox, "Advanced post-processing for scanned ultrasonic arrays: Application to defect detection and classification in non-destructive evaluation", *NDT & E International*, vol. 48, no. 6-7, pp. 636-642, 2008.

[4] D. Colton and A. Kirsch, "A simple method for solving inverse scattering problems in the resonance region", *Inverse Problems*, vol. 12, no. 4, pp. 383, 1996.

[5] D. Colton, M. Piana and R. Potthast, "A simple method using Morozov's discrepancy principle for solving inverse scattering problems", *Inverse Problems*, vol. 13, no. 6, pp. 1477, 1997.

[6] A. Kirsch, "Characterization of the shape of a scattering obstacle using the spectral data of the far field operator", *Inverse Problems*, vol. 14, no. 6, pp. 1489, 1998.

[7] D. Colton, J. Coyle and P. Monk, "Recent Developments in Inverse Acoustic Scattering Theory", *SIAM Rev.*, vol. 42, no.3, pp. 369-414, 2000.

[8] F. Simonetti, "Multiple scattering: The key to unravel the subwavelength world from the far-field pattern of a scattered wave", *Phys. Rev. E.*, vol. 73, no. 3, pp. 36619, 2006.

[9] T. Hutt and F. Simonetti, "Super Resolution Imaging in Elastic Media", *AIP Conference Proc.*, vol. 1335, no. 1, pp. 736, 2011.

[10] C. Fan, M. Pan, F. Luo and B. W. Drinkwater, "Multi-Frequency Time-Reversal-Based Imaging for Ultrasonic Nondestructive Evaluation Using Full Matrix Capture", *IEEE Transactions on Ultrasonics, Ferroelectrics, and Frequency Control*, vol. 61, no. 12, pp. 2067-2074, 2014.

[11] C. Fan, M. Caleap, M. Pan, and B. W. Drinkwater, "A comparison between ultrasonic array beamforming and super resolution imaging algorithms for non-destructive evaluation", *Ultrasonics*, vol.54, no. 7, pp. 1842-1850, 2014.

[12] K. M. Tant, A. J. Mulholland, A. Gachagan, "Application of the Factorisation Method to Limited Aperture Ultrasonic Phased Array Data", *Acta Acustica united with Acustica*, vol. 103, no. 6, pp. 954-966, 2017.

[13] C. Zhang, P. Huthwaite and M. J. S. Lowe, "The Application of the Factorization Method to the Subsurface Imaging of Surface-Breaking Cracks", *IEEE Transactions on Ultrasonics, Ferroelectrics, and Frequency Control*, vol. 65, no. 3, 2018.

[14] T. Hutt, "Towards next generation ultrasonic imaging", UK: Imperial College London, 2011.

[15] I. Virkkunen, "Thermal Fatigue of Austenitic and Duplex Stainless Steels", Finnish Academy of Technology, 2001.

[16] J. Wåle and P. Ekstrøem, "Crack characterisation for in-service inspection planning", SKI Report 95:70, 1995.

[17] J. Wåle, "Crack characterisation for in-service inspection planning – An update", SKI Report 2006:24, 2006.

[18] J. A. Ogilvy, "Wave scattering from rough surfaces", *Rep. Prog. Phys.*, vol.50, no. 12, pp. 1553-1608, 1987.

[19] J. Zhang, B. W. Drinkwater and P. D. Wilcox, "Effect of roughness on imaging and sizing rough crack-like defects using ultrasonic arrays", *IEEE Transactions on Ultrasonics, Ferroelectrics, and Frequency Control*, vol. 59, no. 5, 2012.

[20] J. A. Greenwood, "A unified theory of surface roughness", *Proc. R. Soc. A*, vol. 393, no. 1804, pp. 133-157, 1984.

[21] J. A. Ogilvy and H. M. Merklinger, "Theory of Wave Scattering from Random Rough Surfaces", *Journ. Acoustical Soc. America*, vol. 90, no. 6, pp.3382, 1991.

[22] J. R. Pettit, A. E. Walker and M. J. S. Lowe, "Improved detection of rough defects for ultrasonic nondestructive evaluation inspections based on finite element modeling of elastic wave scattering", *IEEE Transactions on Ultrasonics, Ferroelectrics, and Frequency Control*, vol. 62, no. 10, pp. 1797-1808 2015.

[23] J. A. Ogilvy, "Computer simulation of acoustic wave scattering from rough surfaces", *J. Phys. D: Appl. Phys.*, 21:260–277, 1988.

[24] S. K. Lehman and A. J. Devaney, "Transmission mode time-reversal super-resolution imaging", *Journ. Acoustical Soc. America*, vol. 113, no. 5, pp. 2742-2753, 2003.

[25] Y. Labyed and L. Huang, "Ultrasound time-reversal MUSIC imaging of extended targets", *Ultrasound in Medicine & Biology*, vol. 38, no. 11, pp. 2018-2030, 2012.

[26] H. Lev-Ari and A. J. Devaney, "The time-reversal technique re-interpreted: Subspace-based signal processing for multi-static target location", *Proceedings of the 2000 IEEE Sensor Array and Multichannel Signal Processing Workshop. SAM 2000*, pp. 509–513, 2000.

[27] P. Huthwaite, "Accelerated finite element elastodynamic simulations using the GPU", *J. Comput. Phys.*, vol. 257, Part A, pp. 686-707, 2014.

[28] M. Israeli and S. A. Orszag, "Approximation of radiation boundary conditions", *J. Comput. Phys.*, vol. 41, no. 1, pp. 115-135, 1981.

[29] P. Rajagopal, M. Drozdz, E. A. Skelton, M. J. Lowe, and R. V. Craster, "On the use of absorbing layers to simulate the propagation of elastic waves in unbounded isotropic media using commercially available finite element packages", *NDT & E International*, vol. 51, pp. 30-40, 2012.

[30] M. B. Drozdz, "Efficient finite element modelling of ultrasound waves in elastic media", UK: Imperial College London, 2008.